International Journal of Multiphase Flow 56 (2013) 105–118

Contents lists available at SciVerse ScienceDirect

International Journal of Multiphase Flow

journal homepage: www.elsevier.com/locate/ijmulflow

Numerical simulation of the modulated flow pattern for vertical upflows by the phase separation concept

Qicheng Chen [a], Jinliang Xu [a,b,*], Dongliang Sun [b,c], Zhen Cao [c], Jian Xie [b], Feng Xing [c]

[a] State Key Laboratory of Alternate Electrical Power System with Renewable Energy Sources, North China Electric Power University, Beijing 102206, China
[b] The Beijing Key Laboratory of Multiphase Flow and Heat Transfer, North China Electric Power University, Beijing 102206, China
[c] The Beijing Key Laboratory of New and Renewable Energy, North China Electric Power University, Beijing 102206, China

ARTICLE INFO

Article history:
Received 12 December 2012
Received in revised form 15 May 2013
Accepted 21 May 2013
Available online 7 June 2013

Keywords:
Phase separation concept
Mesh cylinder
Numerical simulation
Liquid film thickness
Liquid circulation

ABSTRACT

The multiphase heat transfer could be enhanced by creating thin liquid film on the wall. The phase separation concept is called due to the separated flow paths of liquid and gas over the tube cross section to yield thin liquid film. Our proposed heat transfer tube consists of an annular region close to the wall and a core region, interfaced by a suspending mesh cylinder in the tube. The heat transfer tube is a multiscale system with micron scale of mesh pores, miniature scale of annular region and macroscale of tube diameter and length. Great effort has been made to link from micron scale to macroscale. The Volume of Fluid (VOF) method simulates air/water two-phase flow for vertical upflow. The three-dimensional system was successfully converted to a two-dimensional one by using three equivalent criteria for mesh pores. The non-uniform base grid generation and dynamic grid adaption method capture the bubble interface. The numerical results successfully reproduce our experimental results. The numerical findings identify the following mechanisms for the enhanced heat transfer: (a) counter-current flow exists with upward flow in the annular region and downward flow in the core region; (b) void fractions are exact zero in the core region and higher in the annular region; (c) the liquid film thicknesses are decreased to 1/6–1/3 of those in the bare tube section; (d) the gas–liquid mixture travels much faster in the annular region than in the bare tube; (e) three-levels of liquid circulation exists: meter-scale bulk liquid circulation, moderate-scale liquid circulation around a single-elongated-ring-slug-bubble, and microliquid circulation following the ring-slug-bubble tails. These liquid circulations promote the fluid mixing over the whole tube length and within the radial direction. The modulated parameters of void fractions, velocities and liquid film thicknesses in the annular region and three-levels of liquid circulation are greatly beneficial for the multiphase heat transfer enhancement.

1. Introduction

Assuming linear temperature distribution within a laminar liquid film, the condensation heat transfer coefficient is $h = k_l/\delta$, where k_l and δ are the liquid thermal conductivity and film thickness. Enhancement of condensation heat transfer focuses on the reduction of the liquid film thickness. Dobson and Chato (1998) noted that the heat transfer mechanisms are strongly related to the flow patterns. This leads to many studies aimed at predicting what dimensionless parameters govern specific flow pattern transitions, and at what values of these dimensionless parameters certain transitions are expected to occur. The heat transfer behavior depends on the flow pattern and particularly on the relative importance of inertial and gravitational forces on the liquid film (Cavallini et al., 2003). Lips and Meyer (2012) performed an experimental study of convective condensation of R134a in an 8.38 mm inner diameter smooth tube in inclined orientations. They presented flow patterns and heat transfer coefficients during condensation for different mass fluxes and vapor qualities over the whole range of inclination angles (from vertical downwards to vertical upwards). The heat transfer coefficient is found to be strongly affected by the liquid and vapor distributions and especially by the liquid thickness at the tube bottom for stratified flows. The flow pattern based heat transfer analysis for the condensation heat transfer can be found in Thome (2003).

Conventionally, the condensation heat transfer can be enhanced by the microstructures fabricated on the wall surface. Microgroove tubes (Graham et al., 1998), micro-fin tubes (Cavallini et al., 2000), herringbone tubes (Miyara and Otsubo, 2002), helically corrugated tubes (Suriyan and Somchai, 2010) belong to the enhanced condenser tubes. The heat transfer enhancement mechanism is

* Corresponding author at: State Key Laboratory of Alternate Electrical Power System with Renewable Energy Sources, North China Electric Power University, Beijing 102206, China. Tel.: +86 10 61772268.
E-mail address: xjl@ncepu.edu.cn (J. Xu).

0301-9322/$ - see front matter © 2013 Elsevier Ltd. All rights reserved.
http://dx.doi.org/10.1016/j.ijmultiphaseflow.2013.05.014

attributed by mixing the fluid boundary layers and limiting the growth of fluid boundary layers close to the wall surface. Physically, the synergy (coordination) of the flow pattern and heat transfer is the key scientific issue of the condensation heat transfer. Usually, void fractions are larger at the tube centerline and are decreased away from the tube centerline, indicating the phase distribution of "gas in the tube core and liquid near the tube wall". This involves large liquid thickness near the wall to deteriorate the heat transfer. It is concluded that the phase distribution does not coordinate with the heat transfer in a conventional tube.

Recently, the flow pattern modulation by the phase separation concept was proposed by our group (Chen et al. 2012). We suspended an empty mesh cylinder in a condenser tube, dividing the tube cross section into an annular region and a core region. Gas bubbles are prevented entering the mesh cylinder thus they are flowing in the annular region to form the thin liquid film. Liquid, however, can be pushed toward the mesh cylinder inside. Air/water two-phase flow experiment was performed in a horizontal tube to verify the fresh idea. Results show that all liquid can be within the mesh cylinder, inducing the whole inner tube surface exposed in gas phase, for a relatively higher liquid height in the horizontal tube. When plug flow interacts with the mesh cylinder surface, elongated saddle bubble train existed in the annular region. All the gas flow rate is flowing in the annular region and the mesh cylinder inside is the liquid.

We note that our flow pattern modulation concept is also useful for the evaporation heat transfer in tubes due to the thin liquid film on the wall. Many authors performed studies on the liquid film thickness (Han and Shikazono, 2009; Han and Shikazono, 2010; Fan et al., 2010; Han et al., 2012). Few studies were reported on how to create the thin liquid film heat transfer mode in tubes.

Here we focused on the numerical simulation of the flow pattern modulation in tubes. A three-dimensional heat transfer tube was successfully converted into a two-dimensional one by using three equivalent criteria for mesh pores. The vertical upflow is considered. Great effort has been made using the non-uniform base grid and dynamic grid adaption methods. The Volume of Fluid (VOF) method simulates the problem. The simulation results were compared with our measured slug bubble lengths and bubble traveling velocities in both the bare tube section and modulated flow section. The modulated flow filed, liquid film thickness and other parameters are successfully obtained for the first time.

2. The phase separation condenser tube

We consider the forced convective condensation heat transfer in a horizontal tube shown in Fig. 1. A constant mass flux of slightly superheated vapor enters the tube which is cooled on the outside wall. The vapor will be thoroughly condensed to liquid assuming a sufficiently long tube. The flow evolves several flow patterns as annular flow and intermittent (slug, plug and bubble) flow consecutively along the flow direction. The annular flow maintains a higher heat transfer coefficient at the tube upstream due to the thin liquid film. However, a big issue is the thick liquid film thickness for the intermittent (slug, plug and bubble) flow to deteriorate the heat transfer, yielding the gradually decreased heat transfer coefficients along the flow length. Void fractions are larger in the tube core and lower near the wall. The condensation heat transfer should be enhanced. For instance, the condensation heat transfer coefficients with organic fluids can be lower than those of cooling water at the outside tube annular.

Fig. 2 shows the proposed phase separation condenser tube, which is so called due to the separated flow paths of gas phase flowing near the tube wall and liquid phase flowing in the tube core. The design consists of a bare tube section (region 1) and a modulated flow pattern section (including a core region 2 and an annular region 3). Because the annular flow possesses higher heat transfer coefficient, the modulated flow section starts from a specific distance away from the tube inlet. Another reason for the bare tube section arrangement is to compare the bubble dynamics between the modulated flow section and bare tube section. Regions 2 and 3 are interfaced by a mesh cylinder surface 4. The mesh cylinder has a flat bottom mesh screen surface and a circular side mesh screen surface. Exit of the mesh cylinder is open. The core region is empty.

The proposed condenser tube works under the forced convective condition. Even though a constant mass flux is given at the inlet, the flow is a transient one due to the varied vapor–liquid interface versus time and space locations (bubble tracking). For horizontal flows, the flow behaves the three-dimensional characteristic due to the non-uniform phase distribution over the tube cross section. The gravity force makes gas phase populated at the tube top and liquid phase populated at the tube bottom (see Fig. 1). The vertical flow can be simplified as a two-dimensional one due to the uniform phase distribution along the tube circumference direction, by the 3-D to 2-D conversion of mesh pores described in the next section.

The proposed condenser tube confines bubbles in the annular region (region 3 in Fig. 2) to form the thin liquid film on the wall. We gave the fundamental analysis of bubble confinement in the annular region and liquid flow across the mesh pores here.

2.1. Mesh pores prevent gas bubbles entering the core region

Two mechanisms govern the mass and momentum exchanges across the mesh pores. When a single-phase stream (either gas or liquid) is continuously interacting with the mesh pores, the mass and momentum transfer across the two sides of mesh pores obeys the pressure driven flow principle. The flow is dependent on the pressure difference and flow field across the annular region and core region, under which nothing prevents gas or liquid flowing across the mesh pores.

Another mechanism concerns an intermittent flow (plug, slug or bubble) approaching the mesh screen surface. Bubbles are difficult to enter the mesh pores if the mesh pores are sufficiently small. This is because the surface energy of gas bubble should be increased when the bubble interface moves from a larger space

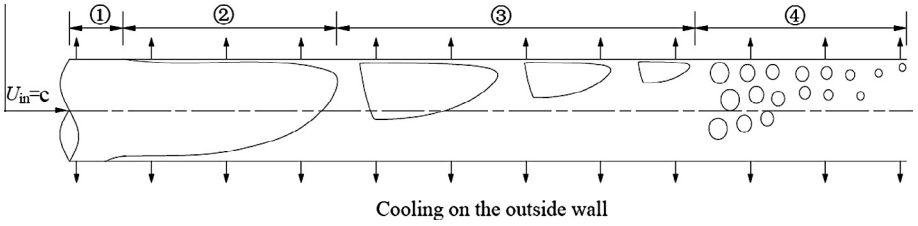

Fig. 1. The flow pattern evolution along a conventional condenser tube (horizontal position, non-uniform phase distribution over tube cross section, 1: superheated vapor flow, 2: annular flow, 3: intermittent flow, 4: bubble flow).

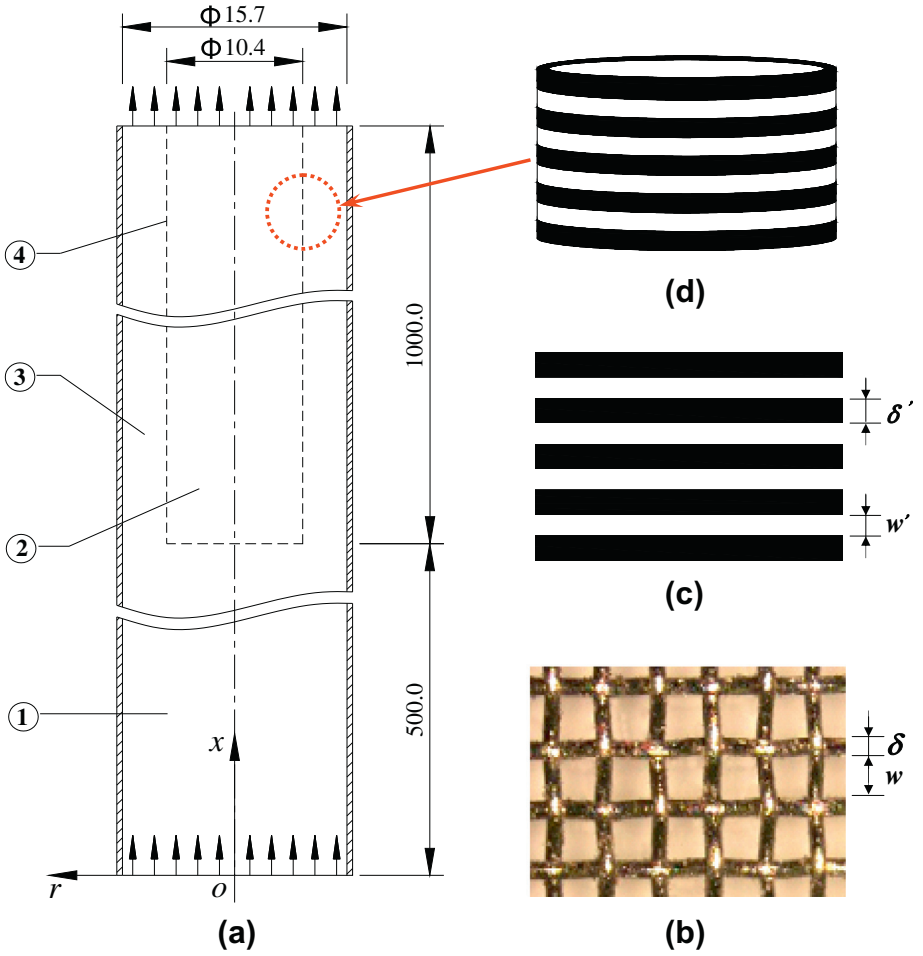

Fig. 2. The configuration of the enhanced heat transfer tube and 3-D to 2-D conversion of mesh pores (a: the tube configuration, 1, bare tube section, 2, core region, 3, annular region, 4, mesh cylinder; b: picture of the stainless steel mesh screen; c: equivalent stripe-type mesh pores; and d: winding of the stripe-type mesh pores. All dimensions are in millimeter).

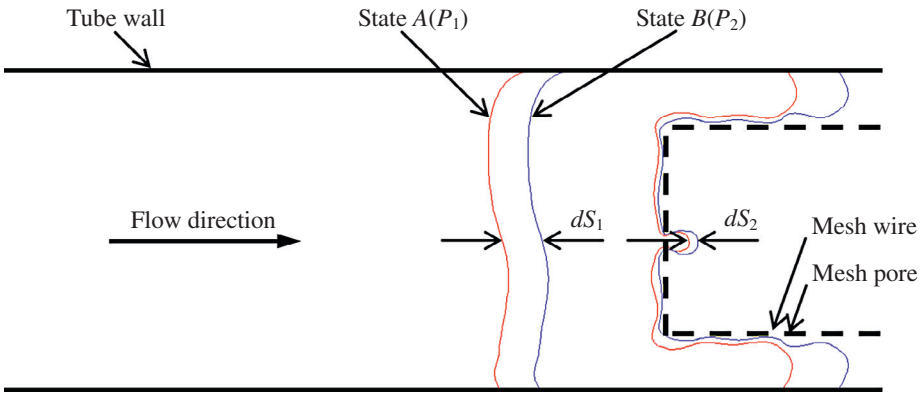

Fig. 3. The pressure difference analysis for a bubble penetrating over the mesh pore (the red color represents the bubble at the initial state *A*, the blue color represents the bubble at the ending state *B*). (For interpretation of the references to color in this figure legend, the reader is referred to the web version of this article.)

into a smaller space. Considering a large bubble with its diameter identical to the condenser tube is penetrating a square mesh pore (see Fig. 3), the surface energy of the gas bubble between state *A* (initial state) and *B* (ending state) is

$$dE = 4\sigma w\, ds_2 - \sigma\pi D\, ds_1 \tag{1}$$

where E is the surface energy, σ is the surface tension, w is the square pore width, D is the tube inner diameter, $\pi = 3.14$, ds_1 is the moving distance from state *A* to *B* in the bare tube, ds_2 is that within mesh pores (see Fig. 3). The mass conservation for the gas bubble yields

$$w^2 ds_2 = \frac{\pi D^2}{4} ds_1 \tag{2}$$

Thus the work required to transform the gas bubble from state *A* to *B* is

$$dK = P_1 \frac{\pi D^2}{4} ds_1 - P_2 w^2 ds_2 \quad (3)$$

where W is the work, P_1 and P_2 are the gas bubble pressures at the state A and B respectively. We have the following equation with $dK = dE$

$$P_1 - P_2 = 4\sigma\left(\frac{1}{w} - \frac{1}{D}\right) \quad (4)$$

Eq. (4) illustrates that because $D \gg w$, the second term of the right side of Eq. (4) contributes less to the pressure difference. Giving $\sigma = 0.07275$ N/m for air–water system at 20 °C and $w = 150$ μm, $P_1 - P_2 = 1.94$ kPa, indicating a pressure difference of about 2 kPa required to penetrate a bubble interface within mesh pores.

Similarly, if a bubble in the annular region of the condenser tube is penetrating a mesh pore, the pressure difference can be deduced as (Tsai and Lin, 2002)

$$P_1 - P_2 = 4\sigma\left(\frac{1}{w} - \frac{1}{\delta_a}\right) \quad (5)$$

where δ_a is the annular gap ($\delta_a = 2.65$ mm here). Because δ_a is about eighteen times of w, $P_1 - P_2$ is also on the order of 2 kPa. In summary, a large pressure difference is needed to penetrate a bubble interface within mesh pores. The pressure difference is strongly related to the pore size. The smaller the mesh pores, the larger the pressure difference is. This is the major mechanism for mesh screens to prevent gas bubbles entering the core region.

It is noted that the mesh pores have the micron size, at which the surface tension force is important and continuum fluid mechanics is still valid. This mechanism is thoroughly different from fluids flowing through membrane with nano-pore size. The flow is characterized by the Knudsen number: $Kn = \lambda/L$, where λ is the average molecule free length and L is the nano-pore size. Gas may travel in nano-pores faster than liquid due to the smaller flow resistance of gas in nano-pores.

2.2. Liquid flow through mesh pores

Considering a liquid droplet in a gas environment, droplet and gas are the disperse phase and continuous phase respectively. When the droplet is attacking a solid surface without holes within, a hydrophilic surface yields a contact angle of smaller than 90°, and a hydrophobic surface yields a contact angle of larger than 90°. The situation is changed when a liquid droplet is attacking a mesh screen surface. We impinged a 5.0 mm diameter water droplet on a mesh screen surface, which was identical to that used for the flow pattern experiment and numerical simulation. Fig. 4 shows the quick droplet spreading to a diameter of 9.74 mm in 0.4 s. It is observed by the microscope that the liquid is thoroughly within mesh pores and liquid never accumulates on the mesh screen surface as a droplet form. Thus the mesh screen surface is a thoroughly hydrophilic surface due to the capillary pumping effect within mesh pores. A droplet formed on a solid surface without pores is caused by the contact angle effect.

The present application involves the continuous phase of liquid and disperse phase of gas, implying liquid droplet not existing in the system. Gas is flowing in the bare tube and modulated flow sections as a consecutive bubble train. Section 5 will show that liquid flow cannot be established when the bubble interface is approaching the mesh pores. This is because a liquid film underneath the bubble interface "blocks" the mesh pores. However, if a bubble interface is far away from the mesh pore, liquid flow can be established across the two sides of mesh pores, obeying the pressure driven flow principle. Such condition exists when both the annular region and core region are liquids at the local tube cross section.

3. The physical problem

This work simulates a forced convective gas–liquid flow (recall Fig. 2), which is a transient flow problem due to the varied phase distribution versus time and space locations. The vertical up flow is considered because this can be simplified as a two-dimensional problem, by performing the 3-D to 2-D conversion of mesh pores.

3.1. The 3-D to 2-D conversion of mesh pores

The enhanced condenser tube is a three-level multiscale system: (1) micron scale of the mesh pores; (2) miniature scale of the annular region; and (3) macroscale of the core region and tube length (meter scale). Assuming a mesh cylinder length of 1.0 m and diameter of 10.4 mm, a metallic wire thickness of 0.07 mm and mesh pore size of 150 μm, the number of mesh pores attains 674,710 (million magnitude). Numerical simulation of such a huge number of mesh pores in micron scale is impossible at this stage. Thus a two-dimensional equivalent system should be developed and a set of equivalent criteria for mesh pores are necessary.

Fig. 2b shows a mesh screen with square mesh pores, having a metallic wire thickness of δ and a mesh pore width of w. Fig. 2a can be simplified to a 2-D system by converting square mesh pores (Fig. 2b) into a stripe-type mesh pores (Fig. 2c). The metal wire thickness is δ' and the stripe-type mesh pore size is w'.

3.1.1. The equal equivalent diameter criterion

The square mesh pore has an equivalent diameter of w, the stripe-type mesh pores has an equivalent diameter of $2w'$. The equal equivalent diameter criterion for both types of mesh pores yields $w' = 0.5w$.

3.1.2. The equal flow area criterion

Remember that the projective area of the total mesh pores (see Fig. 2b) should be equal to that shown in Fig. 2c. The equal flow area criterion gave $[w/(w+\delta)]^2 = w'/(w'+\delta')$. Thus we have $\delta' = \delta + \delta^2/2w$.

3.1.3. The equal capillary pressure criterion

The capillary pressure is important to influence the gas–liquid interface near the mesh pores. The equal capillary pressure criterion is automatically satisfied if the criteria of equal mesh pore diameter and flow area are valid. This is because the capillary pressure created by the square mesh pores is $\Delta p = 4\sigma\cos\theta/w$, which is equal to $\Delta p = 2\sigma\cos\theta/w'$ for the stripe-type mesh pores, where θ is the contact angle.

Winding a large piece of stripe-type mesh screen forms a mesh cylinder (see Fig. 2d). Suspending the mesh cylinder in a tube creates an enhanced heat transfer tube (see Fig. 2a). A 2-D coordinate system is established with r as the radial coordinate and x as the axial coordinate. The bulk flow is upward thus the gravity is against the bulk flow direction.

3.2. The physical problem and boundary conditions

Fig. 5 shows half of the computation domain due to the geometry symmetry. A fully developed laminar velocity profile is applied at the inlet at any time.

$$u = 2u_{in}\left[1 - \left(\frac{r}{R}\right)^2\right] \quad (6)$$

where u_{in} is the average liquid velocity, r is the radial coordinate and R is the tube radius. Sometimes one uses the uniform velocity at the tube inlet. But this does not influence the downstream flow field evolution if the tube is sufficiently long.

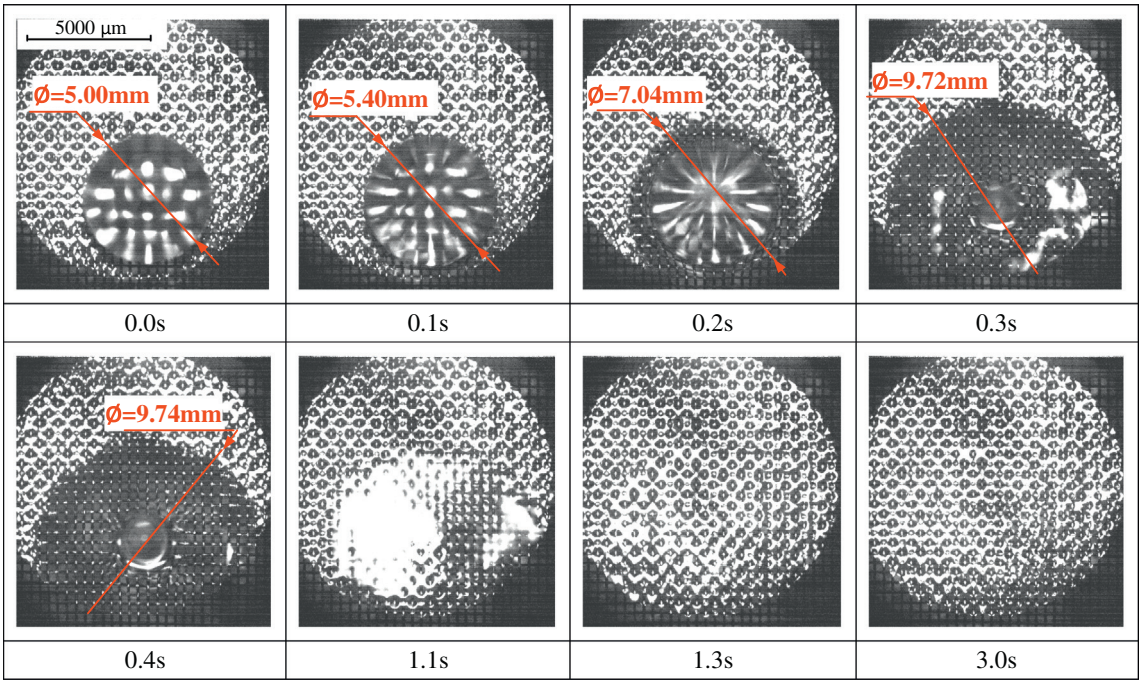

Fig. 4. Quick spreading a water droplet within the mesh screen pores due to the capillary pumping effect.

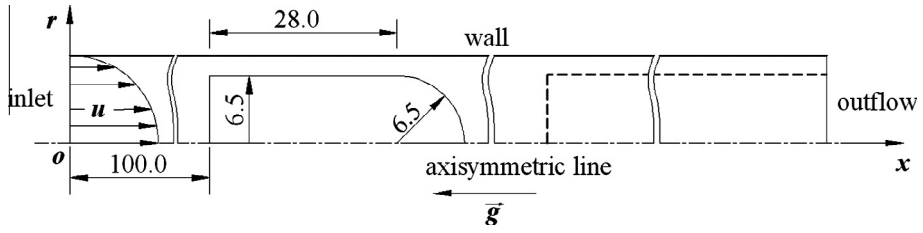

Fig. 5. The physical problem used for numerical simulation (all dimensions are in millimeter).

Once a steady liquid flow is reached within the heat transfer tube, a slug bubble is arranged in the bare tube section (see Fig. 5), with the bubble rear away from the tube inlet of 100.0 mm. The slug bubble has a cylinder body and a half sphere bubble nose. The diameter and length of the cylinder part are 13.0 mm and 28.0 mm, respectively. The half sphere radius is 6.5 mm. In order to create a slug bubble train in the tube, identical slug bubbles are periodically emitted at the same location shown in Fig. 5. The slug bubble generation frequency is f.

The volume flow rates of liquid and gas phases are $Q_l = u_{in}A - V_s f$ and $Q_g = V_s f$ respectively, where A is the tube cross section area and V_s is a single bubble volume. The superficial velocities of liquid and gas phases are defined as

$$J_l = \frac{Q_l}{A} = \frac{u_{in}A - V_s f}{A} \tag{7}$$

$$J_g = \frac{Q_g}{A} = \frac{V_s f}{A} \tag{8}$$

Table 1 summaries the major parameters used for both numerical simulation and experiment. The total number of stripe-type mesh pores attains 6211. The no-slip boundary condition was applied on the tube wall and each metallic wire surface. At the tube outlet (x = 1500 mm), the flow is fully developed, i.e., $\frac{\partial u}{\partial x} = 0$, $\frac{\partial v}{\partial x} = 0$.

4. Numerical method and solution procedure

4.1. Governing equations

The Volume-of-Fluid (VOF) method simulates gas–liquid two-phase flows in the bare tube section and modulated flow section. The method is structured to solve a single momentum equation throughout the domain, while the resulting velocity field is shared among the phases. The governing equations are expressed as follows.

The advection equation of the volume fraction:

$$\frac{\partial \alpha}{\partial t} + \nabla \cdot (\vec{v}\alpha) = 0 \tag{9}$$

The continuity equation:

$$\nabla \cdot \vec{v} = 0 \tag{10}$$

The momentum equation:

$$\frac{\partial}{\partial t}(\rho \vec{v}) + \nabla \cdot (\rho \vec{v}\vec{v}) = -\nabla p + \nabla \cdot [\mu(\nabla \vec{v} + \nabla \vec{v}^T)] + \rho \vec{g} + F_{vol} \tag{11}$$

in which

$$\rho = \rho_l \alpha_l + \rho_g \alpha_g \tag{12}$$

$$\mu = \mu_l \alpha_l + \mu_g \alpha_g \tag{13}$$

Table 1
Major parameters used in this study.

L_b	Bare tube section length	500.0 mm	L_m	Modulated flow section length	1000.0 mm
D	Bare tube diameter	15.7 mm	D_{in}	Mesh cylinder diameter	10.4 mm
δ	Mesh wire thickness	70 μm	w	Square mesh pore width	150 μm
δ'	Stripe-type mesh wire thickness	86 μm	w'	Gap of stripe-type mesh pore	75 μm
u_{in}	Average inlet velocity	0.103 m/s	V_b	A single bubble volume	4.3×10^{-6} m^3
f	Bubble injection frequency	2.07 Hz	J_l and J_g	Superficial velocities of two phases	57.4 and 45.9 mm/s

In Eqs. (9)–(13), α is the void fraction, t is the time, $\vec{v}$ is the velocity vector, ρ and μ are density and viscosity respectively, g is the gravity acceleration ($g = 9.81$ m/s^2). The subscripts l and g denote the liquid and gas phase respectively. The volume force due to the surface tension effect in Eq. (11) is modeled as (Brackbill et al., 1992):

$$F_{vol} = \sigma \frac{\alpha_l \rho_l \kappa_l \nabla \alpha_l + \alpha_g \rho_g \kappa_g \nabla \alpha_g}{0.5(\rho_l + \rho_g)} \tag{14}$$

where σ is the surface tension, κ is the interface curvature having the following expression:

$$\kappa_l = -\kappa_g = -\nabla \cdot \left(\frac{\nabla \alpha_l}{|\nabla \alpha_l|} \right) \tag{15}$$

The contact angle that the fluid makes with the wall boundary adjusts the surface normal in cells near the wall. This dynamic boundary condition results in the curvature adjustment of the surface near the wall. Assuming a contact angle of θ at the wall, the surface normal at the live cell next to the wall is

$$\hat{n} = \hat{n}_w \cos\theta + \hat{t}_w \sin\theta \tag{16}$$

where $\hat{n}_w$ and $\hat{t}_w$ are the unit vectors normal and tangent to the wall, respectively. The wall contact angle is only important when both of the phases contact with the solid wall or the liquid film around the gas bubble is so thin that the van der Waal forces can act across the film. Once a slug bubble is formed with a liquid film on the wall, wall adhesion plays no role to decide the bubble shape. Because the liquid film thicknesses are in the orders of millimeter and 100 μm in the bare tube section and modulated flow section, respectively, the role of the contact angle is negligible in this study. This treatment is similar to that of Mehdizadeh et al. (2011). It is noted that the surface tension force and contact angle are two different concepts. The surface tension force (σ refers to the attractive force across the gas–liquid interface within sub-micron or nanoscale thickness, yielding the volume force F_{vol} (see Eq. (14)) to influence the bubble shape, size and velocity. It has nothing to do with the solid wall.

4.2. The grid generation and interface tracking

Because each mesh pore is involved in the computation, the heat transfer tube is a strong multiscale coupled system. Fig. 6 a shows the base grid generation, which is described as:

- A quasi-uniform grid size of 375 μm is applied along the axial flow direction (not including the near mesh pore region).
- A non-uniform base grid sizes are used along the radial direction, with the coarse grid size of 375 μm in the bulk region, and the finest grid size of 10 μm for the first layer of the tube wall. The grids are gradually refined from the bulk region to the near wall region.
- Grid sizes are significantly refined near the mesh pores. In order to adapt the grid size from the bulk region to the near mesh pore region, the grid sizes are refined by two steps, with fine grid size of 18.75×18.75 μm near and within mesh pores, moderate grid size of 75×75 μm away from the mesh pores, and the normal grid size of 375×375 μm in the bulk region. The fine grid size of 18.75×18.75 μm corresponds to sixteen girds within a mesh pore.

We apply a dynamic grid adaption method to treat the interface tracking. When a slug bubble is traveling in the bare tube section, the grids are automatically refined near the interface (see Fig. 6b). Meanwhile, Fig. 6c shows the significantly refined grids at the bubble front close to the mesh pore surface. The minimum dynamic grid size of 18.75×18.75 μm is reached on such locations. Further grid refinement yields no significant improvement of the computation results.

4.3. Differencing schemes

The finite volume method embedded in FLUENT 6.3.26 was applied to solve Eqs. (9)–(11) and boundary conditions. The second order upwind scheme and SIMPLE algorithm were applied for momentum discretization and pressure–velocity coupling, respectively. A geometric reconstruction scheme captures the interfaces accurately. The time marching of the continuity and momentum equations was fulfilled by a first-order implicit scheme. The time step is controlled by a specified maximum value for the Courant number, which is defined as

$$Co = \frac{\Delta t}{\Delta x / v} \tag{17}$$

where Δx is the grid size and v is the fluid velocity. We set a maximum Courant number of 0.25 and use a variable time step based on the Courant number. Since the grids are very fine close to the interface, the time steps are in the order of 10^{-6}–10^{-5} s. When a slug bubble is crossing the mesh cylinder entrance, the fast interface deformation causes the smallest time step of 10^{-6} s. The simulations are run on a work station having two 8-core CPUs (2.4 GHz each) and 24 GB of RAM. The computation needs about one month.

5. Results and discussion

5.1. Comparison of the numerical results with experiment

Continued from the flow pattern modulation experiment of Chen et al. (2012) for horizontal flows, the vertical upflow experiment was performed to verify the numerical simulations in this paper. The vertical test section was exactly identical to that used for the numerical simulations (see Figs. 2 and 5). The major geometry and running parameters are summarized in Table 1. The air/water two-phase flow loop (Chen et al. 2012) supplies air and water into the vertical test section. Water enters the test section from its inlet as a continuous phase. Air enters the test section as the disperse phase through a needle located 100 mm downstream of the water inlet. Flow rates of water and air were carefully adjusted by two throttle valves in pipelines, and they were measured by two turbine flowmeters, respectively. Both flowmeters have the accuracy of 0.5% in their own flow ranges. The experiment was performed at the room temperature and atmospheric pressure. The bubble

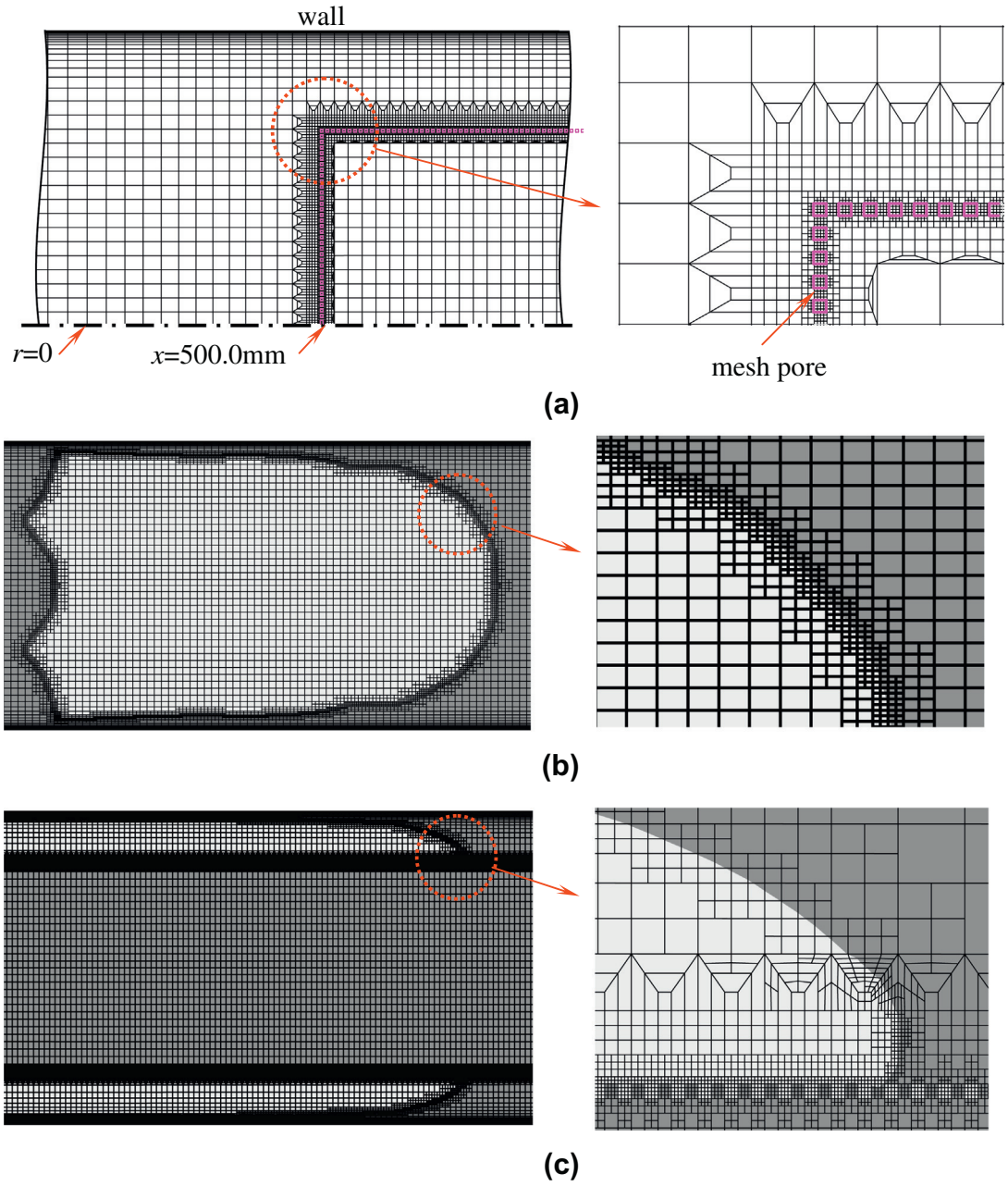

Fig. 6. The base grid generation and dynamic adaption grid generation (a: base grid generation with refined grids near the wall and mesh pores; b: dynamic grid adaption near the bubble interface; and c: dynamic adaption grid generation with significantly refined grids near the bubble interface close to the mesh pores).

shape and size were dynamically visualized by a high speed camera with high accuracy.

Because the numerical simulation including 6211 stripe-type 75 μm mesh pores needs one month, only one case of the experimental data was presented here. But this is enough to demonstrate the major flow pattern modulation mechanisms, incorporating with the numerical findings. The results are demonstrated for the average inlet water velocity of 0.1033 m/s. The slug bubble had a length of 28.0 mm and a diameter of 13.0 mm for the body part and a quasi-half-sphere bubble nose. The bubble generation frequency was $f = 2.07$ Hz. Periodical generation of slug bubbles forms a slug bubble train in the bare tube section.

Note that the length to diameter ratio of 32 for the bare tube section, the slug bubble flow can reach a fully developed situation. Fig. 7a and b shows the slug bubble lengths of 34.0 mm for the measured value and 33.0 mm for the simulated value in the fully developed slug flow region of the bare tube section. They are agreed well with each other. Once a bubble interacts with the mesh cylinder surface, the bubble cannot breakthrough the mesh pores due to a large surface energy required. Thus the bubble is enforced to flow in the annular region in the modulated flow section, forming the elongated-ring-slug-bubble to enclose the mesh cylinder. Fig. 7c shows the measured ring-slug-bubble length of 49.0 mm and Fig. 7 d gave the simulated value of 49.7 mm in the modulated flow section.

Fig. 8a shows the fully developed slug bubbles in the bare tube section (simulation result). The bubble slug and liquid plug have the lengths of 33.0 mm and 71.0 mm respectively (see Fig. 8a). The ring-slug bubble had the length of 49.7 mm in the modulated flow section, which is about 1.5 times of that in the bare tube

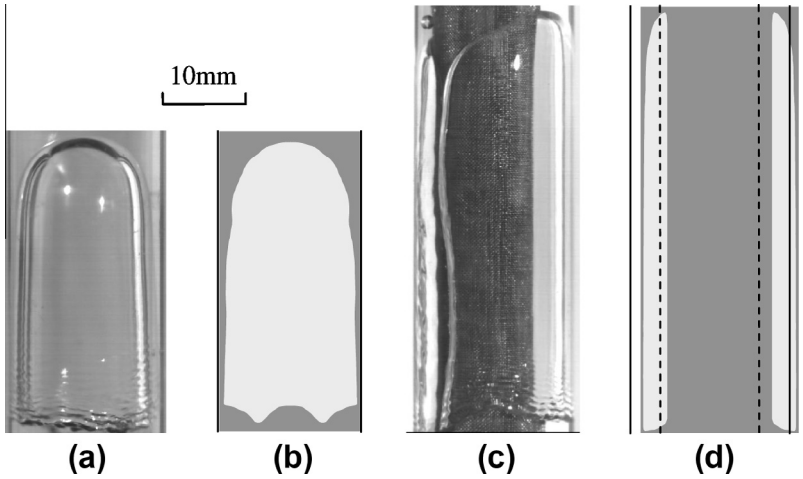

Fig. 7. The bubble shape and length in bare tube section and modulated flow section (a: measured bubble length of $L_{s,m}$ = 34.0 mm in the bare tube section, b: simulated bubble length of $L_{s,s}$ = 33.0 mm in the bare tube section, c: measured elongated-ring-slug-bubble length of $L_{s,m}$ = 49.0 mm in the annular region; and d: simulated elongated-ring-slug-bubble length of $L_{s,s}$ = 49.7 mm in the annular region).

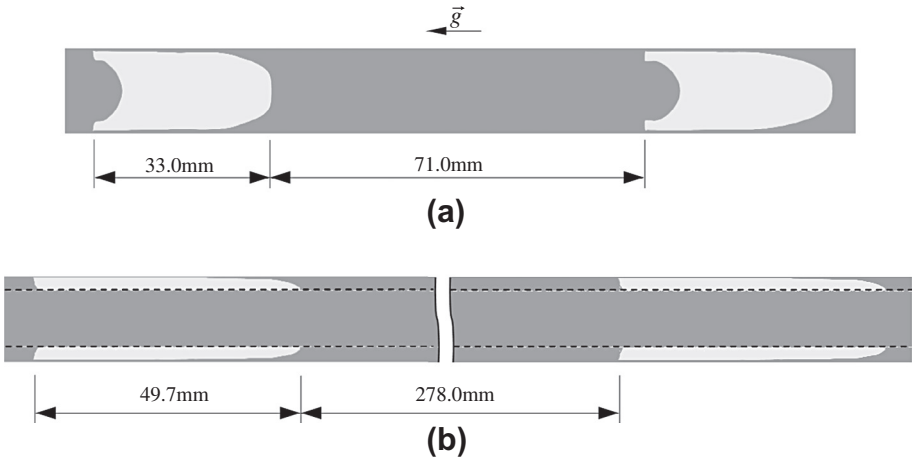

Fig. 8. Lengths of bubble slug and liquid plug in the bare tube section and modulated flow section.

section (see Fig. 8b), due to the bubble confinement in the annular region. The liquid plug is 278.0 mm long in the annular region, which is almost four times of that in the bare tube section.

Fig. 9 shows the simulated and measured bubble traveling velocities in the bare tube section and modulated flow section.

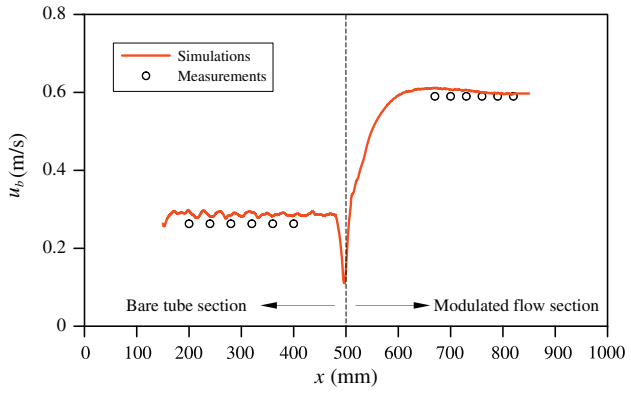

Fig. 9. Bubble traveling velocities (u_b) along the flow direction.

The simulated values are only slightly higher than the measured values, but they are matched well in both flow sections. The numerical simulation gave a steady bubble traveling velocity of 0.29 m/s in the bare tube section. The bubble velocities are sharply decreased and attain the minimal value of 0.11 m/s at the mesh cylinder bottom (x = 500 mm). The bubble is being accelerated within x = 500–600 mm and attains a steady velocity of 0.60 m/s in the annular region. In summary, our numerical simulation linking the micron scale to meter scale could reproduce our experimental results.

5.2. Bubble shape and flow field

Fig. 10 shows the bubble shape and flow field in the bare tube section (Fig. 10a), across the mesh cylinder region (Fig. 10b–d), and in the modulated flow section (Fig. 10e). The pattern was only shown for half of the computation domain for each subfigure due to the geometry symmetry. t was the time for the bubble traveling from the original location (see Fig. 5) to the marked location, x_s and x_e are the locations of bubble tail and bubble nose away from the original coordinate x = 0, respectively. Fig. 10a illustrates the slug bubble and flow field in the bare tube section. At the bubble nose downstream ($x > x_e$), liquids had larger upward velocity in the tube

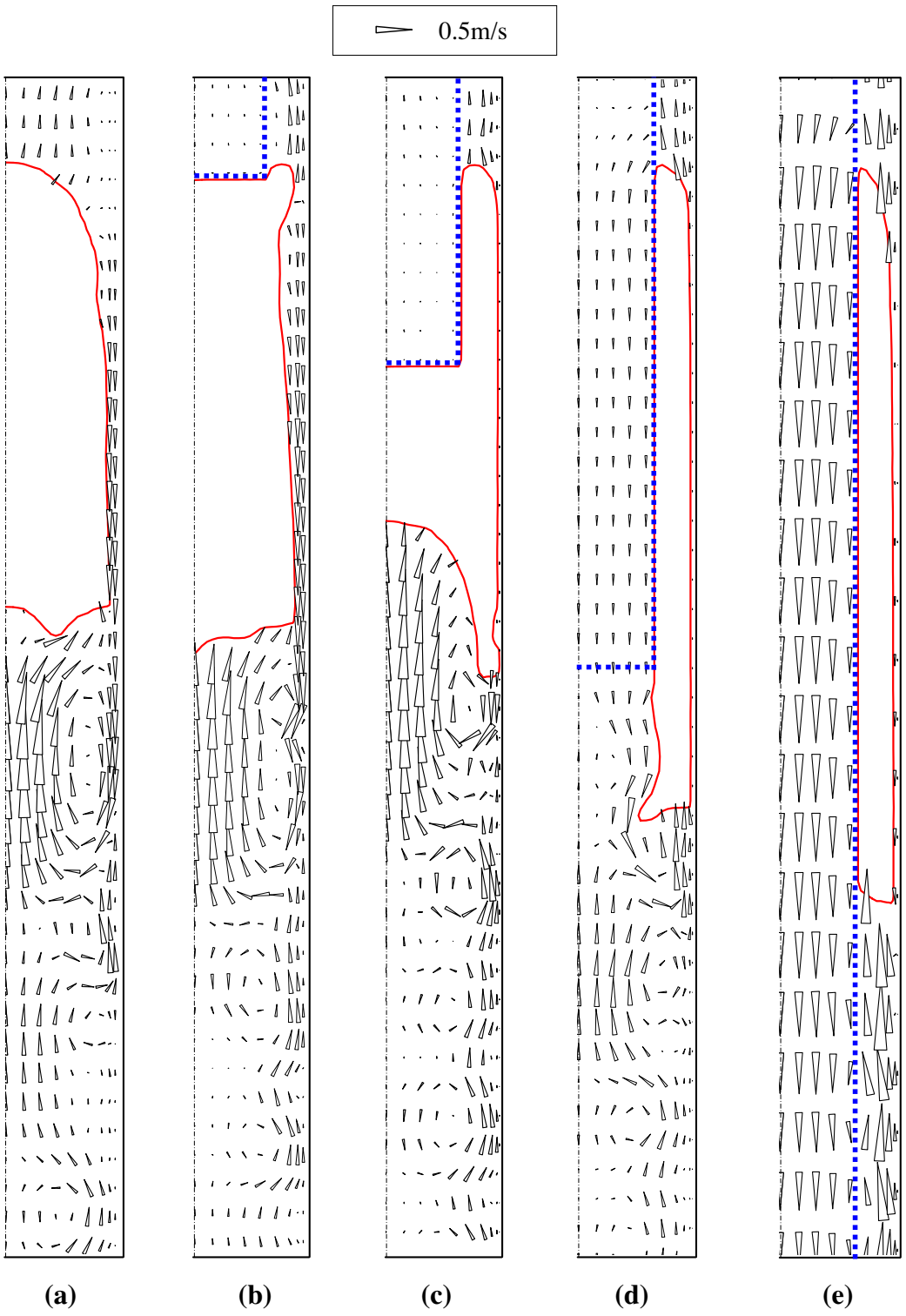

Fig. 10. The velocity field along the flow direction (a: t = 1.737s, x_s = 280 mm, x_e = 313 mm; b: t = 2.624 s, x_s = 467 mm, x_e = 501 mm; c: t = 2.689s, x_s = 479 mm, x_e = 514 mm; d: t = 2.774s, x_s = 491 mm, x_e = 535 mm; e: t = 3.175s, x_s = 716 mm, x_e = 766 mm).

centerline and decreased upward velocity away from the tube centerline. Liquid film enclosing the slug bubble is flowing downwards. An apparent vortex appears below the bubble tail ($x < x_s$). Other vortexes can also be identified but the vortex intensity is weakened with increasing the distance from the slug bubble tail. Many studies have been reported on the slug bubble pattern and flow field (Bugg et al. 1998; Kawaji et al. 1997; Taha and Cui 2004).

Fig. 10b–d demonstrates the pattern for the bubble entering the annular region. Fig. 10b gave the bubble pattern when the bubble front just fully contacts with the mesh cylinder bottom and the O-ring ear begins to form in the annular region. The crossing bubble forms a bubble waist with thick liquid film thickness there. The bubble front interface "blocks" the mesh cylinder bottom, thus liquids near the mesh cylinder bottom are almost stationary. The liquid film is flowing downward, with varied film velocities

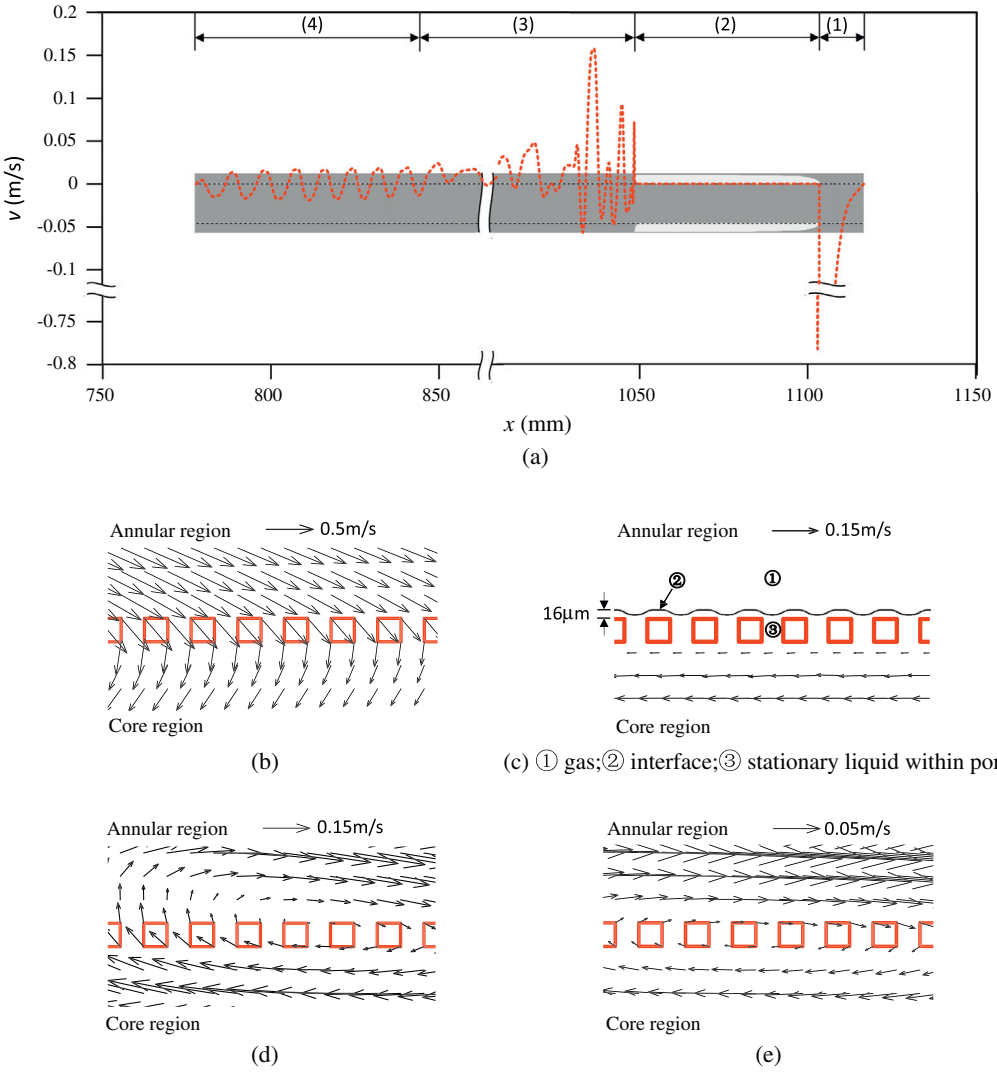

Fig. 11. Radial liquid velocities through mesh pores (b, c, d and e are for flow fields near mesh pores in regions 1, 2, 3 and 4, respectively).

according to the variation of the liquid film thicknesses. Vortexes can be found below the bubble tail, which are similar to those for the slug bubble traveling in the bare tube section.

Fig. 10c shows part of the bubble in the annular region and part of the bubble still in the bare tube section. Again, liquids at the mesh cylinder bottom are stationary due to the mesh pores "sealed" by the bubble interface. A large concave bubble interface forms at the bubble tail due to the liquid inertia force acting on the bubble. The liquid velocity is large inside the concave interface. A set of vortexes appear below the concave bubble interface.

With further bubble traveling downstream, the bubble tail interface is broken to open, causing the downward liquid velocities inside the mesh cylinder (see Fig. 10d). The ring-slug-bubble upward flow in the annular region and the liquid downward flow in the mesh cylinder (core region) form the counter-current flow, which is caused by the buoyancy force due to the large density difference of liquid and gas phases. Fig. 10e identifies a complete elongated-ring-slug-bubble in the annular region. The bulk flow in the annular region is upward, except the downward liquid film flow on the wall. The bulk flow in the core region of the mesh cylinder is downward. It is noted that this is a forced convective flow system. The upflow in the annular region and downflow in the core region are caused by the buoyancy force effect. The net volume flow rate over the whole tube cross section is positive and equals to that at the tube inlet:

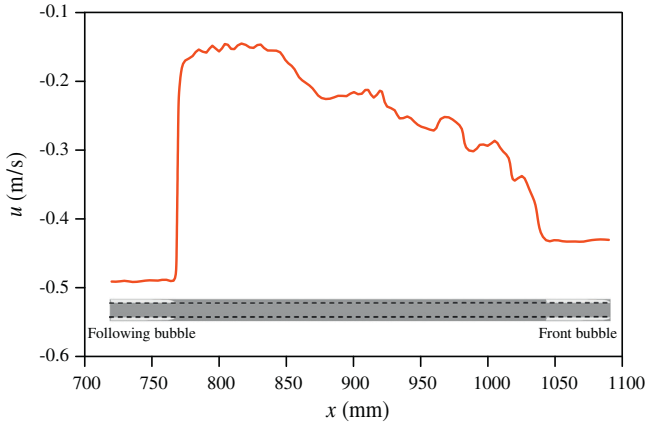

Fig. 12. Liquid axial velocities in the core region along the flow direction.

$$\int_{\text{core region}} 2\pi u r\,dr + \int_{\text{annular region}} 2\pi u r\,dr = \frac{\pi}{4} D^2 u_{in} \tag{18}$$

Alternatively, as a closed flow system, a heat pipe has net zero flow rate over any tube cross section, having counter-current flow inside.

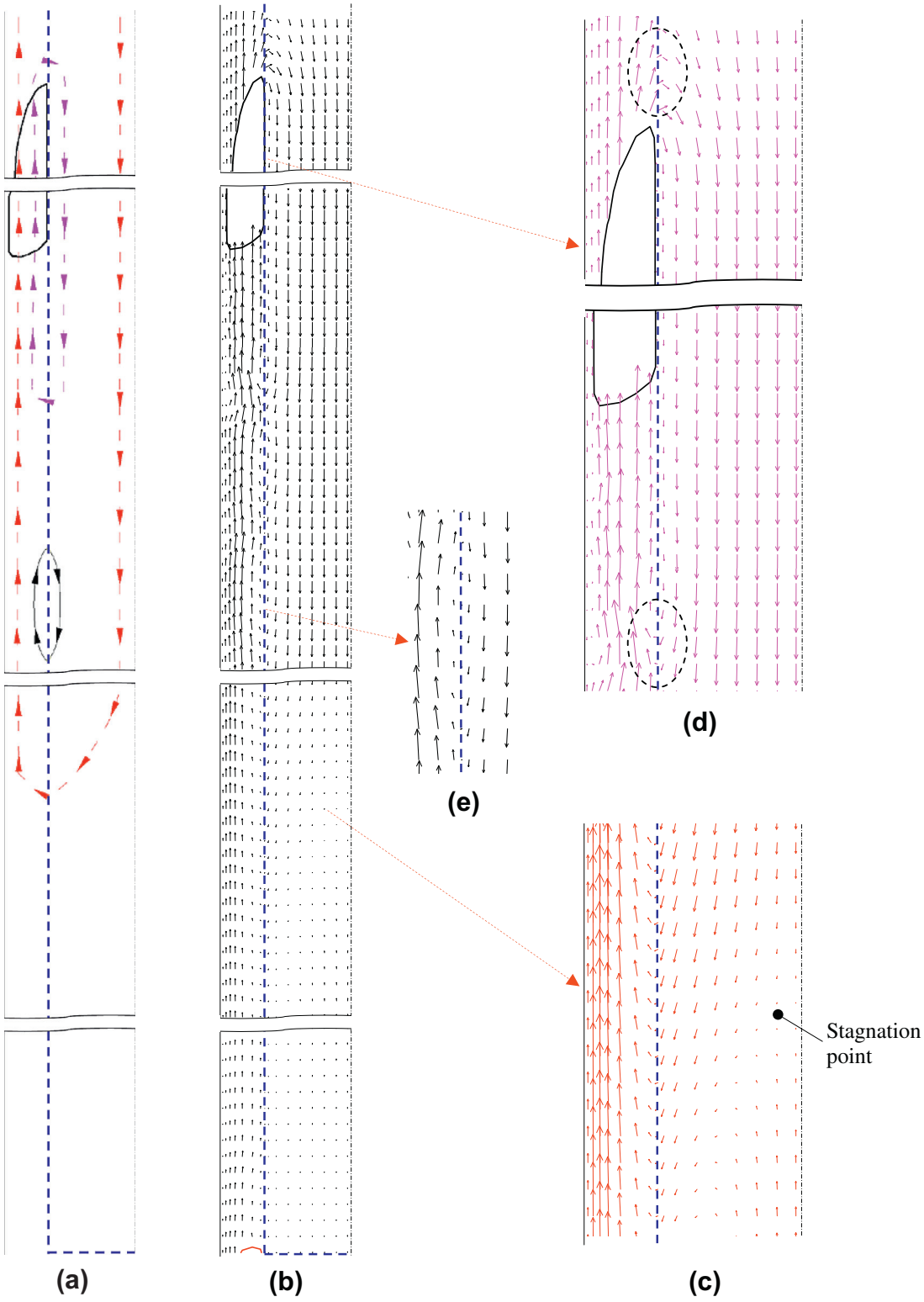

Fig. 13. The whole flow picture.

5.3. Multiscale liquid circulation due to liquid mass exchange through mesh pores

Mesh pores do not allow bubble interface to breakthrough but allow liquid mass exchange. Let us examine the liquid mass exchange around a single ring-slug-bubble first. Fig. 11a shows the radial velocities (v) through mesh pores versus x. The positive sign and negative sign represent the liquid flow from the core region to the annular region and from the annular region to the core region, respectively. Around an elongated-ring-slug-bubble, four regions for the liquid mass exchange are identified:

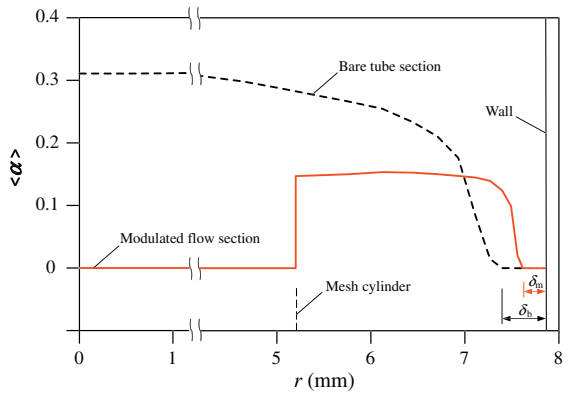

Fig. 14. Void fraction distribution over the tube cross section (δ_m = 0.29 mm is the platform width with liquid on the wall surface for the modulated flow and δ_b = 0.58 mm is the platform width with liquid on the wall surface in the bare tube section).

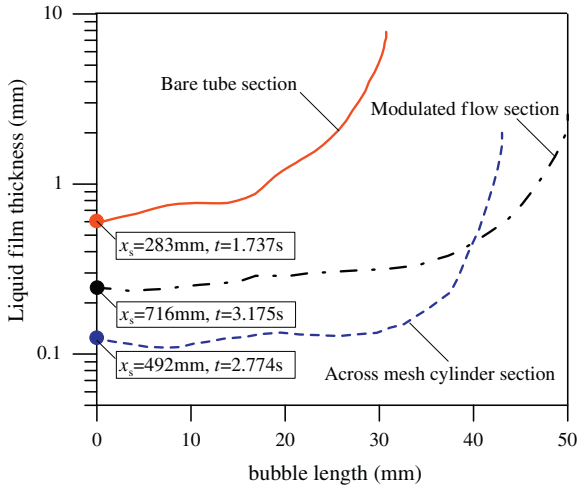

Fig. 15. Liquid film thicknesses in the bare tube section, across the mesh cylinder section and modulated flow section.

- *Region 1*: Liquids are pushed from the annular region to the core region within a short distance of 13 mm at the bubble nose downstream. The maximum (negative) radial velocity reaches 0.78 m/s. Fig. 11 b shows the enlarged flow field near the mesh pores at the bubble nose downstream in region 1.
- *Region 2*: The radial velocity is exact zero in region 2. No liquid mass exchange through mesh pores occurs with mesh pores covered by the ring-slug-bubble body. Fig. 11c shows the enlarged flow field near mesh pores in region 2.
- *Region 3*: Oscillation of radial velocities through mesh pores was identified, with net flow from the core region to the annular region (see Fig. 11d). The maximum positive radial velocity reaches 0.16 m/s, while the maximum (negative) radial velocity reaches 0.06 m/s.
- *Region 4*: Oscillation of radial velocities through mesh pores was identified, with zero net flow through mesh pores. Fig. 11e shows the flow field near the mesh pores.

The flow field near mesh pores identifies and confirms the "check-valve" function of mesh pores. This is an analogy because a real "check-valve" does not exist in the system. As shown in Fig. 11, mesh pores in regions 1, 3 and 4 behave the on-state of the "check-valve", under which mesh pores are thoroughly immersed in liquid and liquid flow can be established driven by pressure difference across the mesh pores. Mesh pores in region 2 behave the off-state of the "check-valve" because there is a gas–liquid interface under the ring-slug bubble. Under such circumstance liquids near mesh pores are stationary and liquid flow cannot be established across mesh pores. We also note that the liquid film thickness between the gas–liquid interface and mesh wire surface is about 16 μm (see Fig. 11c), which is significantly larger than the sub-micron or nanoscale, confirming that the contact angle is not important in this study.

The liquid mass exchange in regions 1 and 3 constructs the liquid circulation around a single ring-slug-bubble. Liquid consecutively flows from the annular region at the bubble nose downstream to the annular region ahead of the ring-slug-bubble tail, through the core region. The liquid mass flow rate towards the core region at the bubble nose is larger than that towards the annular region at the bubble tail, causing the liquid speeding up in the core region (inside mesh cylinder) along the downward flow direction. This liquid circulation happens in the bubble length scale of 10–100 mm. The liquid mass exchange in region 4 constitutes the microliquid circulation, taking place in the length scale of micron-millimeter.

Fig. 12 illustrates the liquid axial velocities in the core region (inside mesh cylinder). The negative sign means the downward flow. The axial velocities are averaged over the cross section of the core region. The axial velocities were plotted between two consecutive ring-slug-bubbles. Along the downward flow direction (from large x to small x), the axial velocities are (a) constant with the annular region covered by the front bubble, corresponding to region 2 in Fig. 11; (b) decreased due to the radial flow from the core region to the annular region, corresponding to region 3 in Fig. 11; (c) constant due to the zero net liquid mass exchange through mesh pores, corresponding to region 4 in Fig. 11; and (d) sharply increased due to the radial liquid flow toward the core region at the following bubble nose downstream, corresponding to region 1 in Fig. 11.

Fig. 13 summaries the whole flow picture. Because the heat transfer tube has significantly large tube length to diameter ratio, the flow field was plotted over different subsections, but this is enough to demonstrate the flow picture over an entire tube length. Fig. 13a qualitatively shows the flow picture, with bulk circulation marked by the red color, circulation around a single ring-slug-bubble with the pink color, and microcirculation with the black color, respectively. Fig. 13b gave the flow field over different subsections.

5.3.1. Meter-scale bulk liquid circulation

The bulk liquid circulation is formed between the upward flow in the annular region and the downward flow in the core region, starting from the liquid flow from the annular region near the tube outlet to the mesh cylinder bottom area. The bulk circulation is caused by the heavy liquid in the core region and light fluid mixture in the annular region, taking place along the whole tube length in meter scale. There is a stagnation point near the mesh cylinder bottom, above which the flow is downward and below which the flow is upward (see Fig. 13c).

5.3.2. Moderate-scale liquid circulation around a single bubble

The liquid flow rate from the annular region to the core region at the bubble nose downstream is larger than that from the core region to the annular region ahead of the ring-slug-bubble tail, taking place in the bubble length scale of 10–100 mm (see Fig. 13d).

5.3.3. Microscale liquid circulation

There exists local liquid circulation at the bubble tail, taking place in the micron-millimeter scale (see Figs. 11e and 13e).

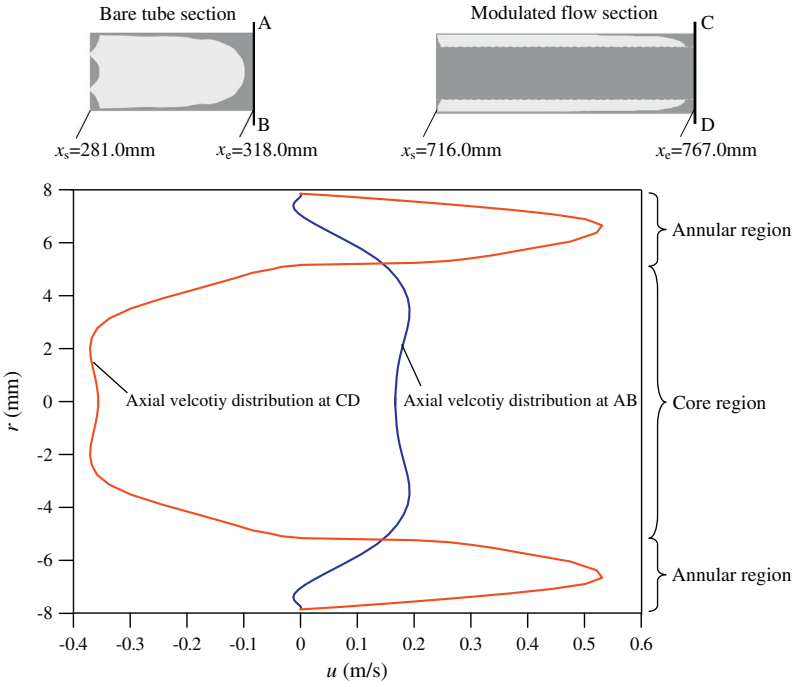

Fig. 16. Axial velocity (u) distributions over the tube cross section for the bare tube flow and modulated flow.

5.4. Modulated flow parameters due to the separated flow paths of gas and liquid

We apply the flow path separation of liquid and gas phases by suspending a mesh cylinder in a tube. The gas bubbles are flowing in the annular region, while inside of the mesh cylinder is liquid. The phase distribution over the tube cross section is totally different from that in a bare tube. The time-averaged-void-fraction $\langle\alpha\rangle$ is defined as the integrated time with the grid cell occupied by the gas phase divided by the total time. Fig. 14 shows the void fraction distribution over the tube cross section in the bare tube section and modulated flow section respectively. With flows in the bare tube, $\langle\alpha\rangle$ is larger in the major part of the tube cross section, but is decreased near the tube wall. The phase distribution is totally changed by the phase separation concept. Void fractions are exact zero in the core region but have a higher distribution in the annular region, leaving a thin liquid film thickness on the wall. There is a platform near the wall on which liquids are accumulated. The platform thickness is 0.29 mm for the modulated flow and 0.58 mm for the bare tube flow.

Fig. 15 tracks[1] the liquid film thicknesses for a single bubble flowing in different axial locations, noting the mesh cylinder bottom at x = 500 mm. When the bubble is flowing in the bare tube, the liquid film thicknesses are in the range of 0.60–1.20 mm for the slug bubble body (not including the bubble nose, see the red curve of Fig. 15). The bubble front in the annular region and bubble tail in the bare tube section (x_s = 492 mm) represent the crossing bubble state, under which the liquid film thicknesses are in the range of 0.10–0.20 mm within an axial length of 35 mm (see the blue curve of Fig. 15). When an elongated-ring-slug-bubble is completely formed in the annular region, the liquid film thicknesses are in the range of 0.20–0.40 mm for the ring-slug-bubble body (see the black curve of Fig. 15). The liquid film thicknesses for the crossing bubble and flowing bubble in the annular region are significantly decreased compared to those in the bare tube. The heat transfer tube modulated the liquid film thickness to be 1/6–1/3 of those in the bare tube section.

Fig. 16 compares the axial velocity distributions over the tube cross section in the bare tube section and modulated flow section, respectively. The cross sections AB and CD are selected at the bubble nose downstream. For the flow in the bare tube, the axial velocities have positive sign (upward flow), except the negative velocity near the wall. Besides, the axial velocities are smaller near the wall than those in the bulk flow region. The phase separation concept significantly changes the axial velocity distribution over the tube cross section. The axial velocities are significantly larger in the annular region close to the wall, sharply decreased across the mesh screen surface to the negative sign (downward flow) in the core region. The maximum axial velocities are 0.53 m/s for upward flow in the annular region, and about 0.37 m/s for the downward flow in the core region. The modulated axial velocities do behave the inverse distribution as those in the bare tube section.

5.5. Heat transfer enhancement due to the phase separation concept

The phase separation heat transfer tube has wide applications in industries. An example case was taken here. Due to the worldwide energy shortage and environment pollution issues, the Organic Rankine Cycle (ORC) can convert the low grade thermal energy into power or electricity. Evaporator and condenser are major components in the system. Using the organic fluid induces poor phase changer heat transfer in tubes. The proposed concept can make evaporators and condensers with higher heat transfer coefficients, which not only increase the exergy efficiencies of components and system to reach a larger power (electricity) output, but also decrease the investment cost by the decreased heat transfer area, compared with other techniques that were mentioned in the Introduction section. Other applications include the air-conditioners, power plants, etc. Inserting a mesh cylinder in a tube causes a slight increase of the pressure drop. For the case computed in this study, the pressure drop was 7500 Pa/m in the bare tube section, but it was increased by 26.7% to 9500 Pa/m in the

[1] For interpretation of color in Fig. 15, the reader is referred to the web version of this article.

modulated flow section. The enhanced heat transfer mechanism, pressure drop and applications need further detailed study.

Both our experiment and simulation demonstrate that gas is flowing in the annular region and the core region is full of liquid. The following three mechanisms are useful for the multiphase heat transfer enhancement: (1) Void fractions are zero in the core region and larger near the wall, yielding thin liquid film thicknesses on the wall. This is the major heat transfer enhancement mechanism. (2) Both the ring-slug-bubble and liquids are traveling much faster in the annular region. This is the second heat transfer enhancement mechanism. (3) There are three-levels of liquid circulations in the heat transfer system: (a) microscale liquid circulation at the ring-slug-bubble tail in the micron-millimeter scale; (b) moderate-scale liquid circulation around a single-ring-slug-bubble; and (c) meter-scale bulk liquid circulation. The three-levels of liquid circulations significantly enhance the liquid mixing along the radial direction and within the tube outlet and inlet. This is the third heat transfer enhancement mechanism.

6. Conclusions

The following conclusions can be drawn:

- The 3-D heat transfer tube was converted into a 2-D one by using three equivalent criteria for mesh pores.
- The VOF method simulates the problem. The non-uniform base grid generation and dynamic grid adaption methods successfully treat the linking from microscale to macroscale for the enhanced heat transfer tube.
- The simulated bubble lengths and velocities in both the bare tube section and modulated flow section agree well with the measured values.
- The tube behaves the upward mixture flow in the annular region and downward liquid flow in the core region.
- Void fractions are exact zero in the core region and larger in the annular region, indicating the gas phase flowing in the annular region and inside of the mesh cylinder is liquid.
- Liquid film thicknesses are significantly decreased by the modulated flow.
- The fluid mixture travels much faster in the annular region than in the bare tube section.
- The three-levels of liquid circulation promote the liquid mixing over the whole tube length and within the radial direction. These circulations were performed through mesh pores.
- The above mechanisms contribute the heat transfer enhancement.

Acknowledgements

This work was supported by the Natural Science Foundation of China of International Cooperation Project (51210011), the Natural Science Foundation of China (51106049), the National Basic Research Program of China (2011CB710703).

References

Bugg, J.D., Mack, K., Rezkallah, K.S., 1998. A numerical model of Taylor bubbles rising through stagnant liquids in vertical tubes. Int. J. Multiphase Flow 24, 271–281.
Brackbill, J.U., Kothe, D.B., Zemach, C., 1992. A continuum method for modeling surface tension. J. Comput. Phys. 100, 335–354.
Cavallini, A., Del Col, D., Doretti, L., Longo, G.A., Rossetto, L., 2000. Heat transfer and pressure drop during condensation of refrigerants inside horizontal enhanced. Int. J. Refrig. 23, 4–25.
Cavallini, A., Censi, G., Del Col, D., Doretti, L., Longo, G.A., Rossetto, L., Zilio, C., 2003. Condensation inside and outside smooth and enhanced tubes – a review of recent research. Int. J. Refrig. 26, 373–392.
Chen, H.X., Xu, J.L., Li, Z.J., Xing, F., Xie, J., Wang, W., Zhang, W., 2012. Flow pattern modulation in a horizontal tube by the phase separation concept. Int. J. Multiphase Flow 45, 12–23.
Dobson, M.K., Chato, J.C., 1998. Condensation in smooth horizontal tubes. J. Heat Transfer 120, 193–213.
Fan, C., David, M., Wang, F.M., Goodson, K.E., 2010. Influence of film thickness and cross-sectional geometry on hydrophilic microchannel condensation. Int. J. Multiphase Flow 36, 608–619.
Graham, D., Chato, J.C., Newell, T.A., 1998. Heat transfer and pressure drop during condensation of refrigerant 134a in an axially grooved tube. Int. J. Heat Mass Transfer 42, 1935–1944.
Han, Y., Shikazono, N., Kasagi, N., 2012. The effect of liquid film evaporation on flow boiling heat transfer in a micro tube. Int. J. Heat Mass Transfer 55, 547–555.
Han, Y., Shikazono, N., 2009. Measurement of the liquid film thickness in micro tube slug flow. Int. J. Heat Fluid Flow 30, 842–852.
Han, Y., Shikazono, N., 2010. The effect of bubble acceleration on the liquid film thickness in micro tubes. Int. J. Heat Fluid Flow 31, 630–639.
Kawaji, M., Dejesus, J.M., Tudose, G., 1997. Investigation of flow structures in vertical slug flow. Nucl. Eng. Des. 175, 37–48.
Lips, S., Meyer, J.P., 2012. Experimental study of convective condensation in an inclined smooth tube. Part I: Inclination effect on flow pattern and heat transfer coefficient. Int. J. Heat Mass Transfer 55, 395–404.
Mehdizadeh, A., Sherif, S.A., Lear, W.E., 2011. Numerical simulation of thermofluid characteristics of two-phase flow in microchannels. Int. J. Heat Mass Transfer 54, 3457–3465.
Miyara, A., Otsubo, Y., 2002. Condensation heat transfer of herringbone micro fin tubes. Int. J. Therm. Sci. 41, 639–645.
Suriyan, L., Somchai, W., 2010. The effects of corrugation pitch on the condensation heat transfer coefficient and pressure drop of R134a inside horizontal corrugated tube. Int. J. Heat Mass Transfer 53, 2924–2931.
Taha, T., Cui, Z.F., 2004. Hydrodynamics of slug flow inside capillaries. Chem. Eng. Sci. 59, 1181–1190.
Thome, J.R., 2003. Update on advances in flow pattern based two-phase heat transfer models. Exp. Therm. Fluid Sci. 29, 341–349.
Tsai, J.H., Lin, L.W., 2002. Active microfluidic mixer and gas bubble filter driven by thermal bubble micropump. Sensors and Actuators A: Physical 97–98, 665–671.